Journal of Archaeological Science 52 (2014) 84–96

Contents lists available at ScienceDirect

Journal of Archaeological Science

journal homepage: http://www.elsevier.com/locate/jas

New ways to extract archaeological information from hyperspectral pixels

Michael Doneus [a, b, c, *], Geert Verhoeven [b, c], Clement Atzberger [d], Michael Wess [d], Michal Ruš [b]

[a] Department of Prehistoric and Historical Archaeology, University of Vienna, Franz-Klein-Gasse 1, 1190 Wien, Austria
[b] Vienna Institute for Archaeological Science, University of Vienna, Franz-Klein-Gasse 1, 1190 Wien, Austria
[c] LBI for Archaeological Prospection and Virtual Archaeology, Hohe Warte 38, 1190 Wien, Austria
[d] Institute of Surveying, Remote Sensing and Land Information, University of Natural Resources and Life Sciences, Peter Jordan-Straße 82, 1190 Wien, Austria

ARTICLE INFO

Article history:
Received 7 May 2014
Received in revised form
3 July 2014
Accepted 18 August 2014
Available online 27 August 2014

Keywords:
Archaeological prospection
Airborne imaging spectroscopy
High-resolution
Distribution fitting
Red edge inflection point (REIP)
MATLAB®

ABSTRACT

Airborne remote sensing for archaeology is the discipline that encompasses the study of archaeological remains using data collected from an airborne platform by means of digital or film-based aerial photography, airborne laser scanning, hyperspectral imaging etc. So far, airborne hyperspectral scanning or – more accurately – airborne imaging spectroscopy (AIS) has occupied only a very small niche in the field of archaeological remote sensing: besides reasons of cost, the common archaeologically-insufficient ground-sampling distance can be considered the main limiting factor. Moreover, the technical processing of these data sets with a high level of potential redundancy needs specialized software. Typically, calculation of band ratios and a principal component analysis are applied. As a result, the few practical applications of archaeological AIS have not been entirely convincing so far. The aim of this paper is to present new approaches for analysing archaeological AIS data. The imagery under study has a ground-sampling distance of 40 cm and covers the Roman town of *Carnuntum* (Austria). Using two algorithms embedded in a specifically developed MATLAB® toolbox, it will be shown how the extracted archaeological information can be enhanced from high-resolution hyperspectral images. A comparison with simultaneously acquired vertical photographs will indicate the specific advantages of high-resolution AIS data and the gain one can obtain when exploiting its potential using any of the newly presented methods.

1. Introduction

The practice of aerial photographic reconnaissance in which the archaeologist acquires predominantly oblique images from a manned, low-flying aeroplane is still the mostly applied archaeological remote sensing approach. Although this survey approach did not witness major changes over the past century (Verhoeven, 2009), its success lies mainly in its straightforward execution, while its capacity to cover large areas turns it into one of the most cost-effective methods for site discovery. The non-invasive approach also yields easily interpretable imagery with abundant spatial detail (Palmer, 2005; Wilson, 2000). The latter characteristic should never be underestimated, as the spatial resolution of the acquired datasets, which typically is between 5 cm and 10 cm, enables the assessment of small, but often abundant features such as post holes and pits. It can, therefore, be considered one of the main reasons that this type of aerial survey is still so intensely practiced.

Oblique aerial photography does, however, exhibit shortcomings (discussed below in more detail), mainly due to its limited spectral resolving power. Therefore, a growing number of archaeologists are investigating in other aerial archaeology techniques providing images with increased spectral resolution. Although airborne multi-spectral imaging is one of these approaches (e.g. Winterbottom and Dawson, 2005), truly increased spectral resolution is only obtained by airborne hyperspectral scanning (AHS) also called airborne imaging spectroscopy (AIS) (Aqdus et al., 2007, 2008, 2012; Barnes, 2003; Bassani et al., 2009a, 2009b; Bennett et al., 2012, 2013; Cavalli et al., 2007, 2012; Cavalli, 2013; Cavalli and Pignatti, 2001; Challis et al., 2009; Coren et al., 2005;

* Corresponding author. Department of Prehistoric and Historical Archaeology, University of Vienna, Franz-Klein-Gasse 1, 1190 Wien, Austria. Tel.: +43 1 4277 40486; fax: +43 1 4277 9404.
E-mail address: Michael.Doneus@univie.ac.at (M. Doneus).

http://dx.doi.org/10.1016/j.jas.2014.08.023

Emmolo et al., 2004; Forte et al., 2011; Merola, 2005; Merola et al., 2007, 2008; Pietrapertosa et al., 2008; Traviglia, 2005, 2006a, 2006b, 2008; White, 2003). The success rate in terms of detection of archaeological subsurface structures is varying, however, and less successful applications seem to be connected with the lower spatial resolution of the acquired datasets (in most cases ranging from 4 m to – at best – 1 m). Since the current generation of AIS sensors does enable the acquisition of relatively high spatial resolution data (i.e. ground-sampling distance (GSD) below 50 cm), they seem to be promising for archaeological applications.

The high spectral resolution of AIS sensors is generally not easily handled in standard image processing software. Indeed, hyperspectral scans result in huge datasets of hundred and more spectral bands, which are moreover to a high degree correlated and often affected by noise. Processing of these image cubes, i.e. reducing the data to only a few layers containing a high degree of archaeologically relevant information is therefore an important part of the AIS workflow.

In this article, we will present two new approaches that have been developed and tested on comparatively high spatial resolution hyperspectral datasets (GSD $\leq$50 cm). They are implemented in an open MATLAB®-based toolbox called ARTCIS (see Atzberger et al., 2014) and make use of the spectral features stored in the AIS data cube. Therefore, a basic introduction into airborne hyperspectral imaging is provided in the next section (chapter 2), before chapter 3 delves deeper into the two new processing approaches. The proposed approaches are consequently tested on a high-resolution dataset from a case-study area detailed in chapter 4. The results are analysed and discussed in chapters 5 and 6.

2. Airborne imaging spectroscopy

2.1. Limitations of conventional aerial photography

Despite its many advantages and the capability to capture small landscape details, conventional oblique and vertical aerial photography is also characterised by some major spectral shortcomings. In oblique aerial photography, the survey working principles are governed by the human visual system which is only sensitive to the visible electromagnetic spectrum between 400 and 700 nm. Additionally, the majority of the aerial footage has been acquired with photographic media that were sensitised only to this visible radiation (e.g. normal colour photography). Although very striking and revealing images have been obtained in this way, the detection of vegetation marks (and to a certain extent soil marks) becomes impossible in less-optimal circumstances, as the slight differentials of height and colour in crops might exhibit too low a contrast with the surrounding matrix to be noticed through normal (colour) photography in the visible spectrum. Even though researchers have been experimenting with different filters and film emulsions (Crawshaw, 1995) and the application of digital cameras has enabled the easy application of beyond visible imaging in the Near-InfraRed (NIR) domain (Verhoeven, 2012a), visually imperceptible soil and crop disturbances will never be photographed. As an answer to this 'observer-directed' approach (Palmer, 2005), aerial archaeologists have also used photographs generated during strictly vertical sorties (e.g. Coleman, 2007; Doneus, 1997; Kennedy, 1996; Mills, 2005; Palmer, 2007). Although even NIR coverage becomes possible with such a vertical approach, both the standard oblique and vertical photographic strategies still capture reflected solar radiation in spectrally broad wavebands: a typical colour photograph records the visible spectrum in three approximately 100 nm wide channels (Red, Green, Blue), whereas NIR radiation is usually sampled in a 300 nm wide band. This is, however, far from optimal, because particular diagnostic spectral features are often only a few nanometres wide, which makes acquisition of data with a high spectral resolution necessary when one wants to assess small variations in – for example – the plants' physiology. Vertical and oblique photography, even when executed in the spectral range beyond the visible light, thus significantly reduce the diagnostic accuracy of vegetation investigation (Hampton, 1974). In other words, they hamper the detection of archaeological vegetation marks as the reflected radiation is spectrally undersampled and spectral characteristics that are too narrow to be distinguished get masked (Verhoeven, 2009).

Spaceborne data, consistently acquired over extended areas and often in invisible wavebands, have been used in a variety of archaeological surveys (Lasaponara and Masini, 2012). They repeatedly cover large parts of the Earth's surface, are often easily available, and tackle the observer-directed and visible-radiation-limited issues. However, the data are less (or not at all) suited for the discovery and detailed recording of small archaeological features, as the resolving power of the sensors is in all but a few cases more than one meter. Moreover, the spectral bands of older spaceborne imagers (i.e. those whose products are freely available) are generally too broad or misplaced spectrally to truly detect plant stress (Carter, 1994). Airborne multi- and hyperspectral sensors might acquire data in narrow wavebands, but cost, moderate temporal resolution, and low resolving power also significantly hampered their frequent use in archaeological research (Hanson, 2008). An ideal system that joins the best of these approaches by offering the cost-effectiveness as well as operating and post-processing flexibility of the oblique reconnaissance approach, while also allowing a total coverage in narrow visible and invisible spectral wavebands, does not exist so far. However, the current generation of hyperspectral sensors does enable the acquisition of relatively high spatial resolution data (i.e. a GSD below 50 cm) and due to the increased demand in non-archaeological fields, even the acquisition costs are steadily decreasing. However, some big hurdles still need to be taken before these high-resolution AIS data can become of real archaeological interest.

2.2. AIS – what's in a name?

Airborne hyperspectral imaging is a passive remote sensing technique as it digitizes the earth's upwelling electromagnetic radiation (reflected solar radiation or thermal radiation emitted by the objects themselves) in a multitude of small spectral bands. Just as normal photographs consist of a stack of three spatially co-registered two-dimensional images of which each represents the reflected radiation in a broad visible band, the final hyperspectral data product can be considered an extended stack of narrow-band images. Each image is a digitisation of the reflected and/or emitted radiation in a small spectral range (typically around 10 nm in the visible and NIR range). Commonly an airborne hyperspectral flight yields tens to hundreds of these narrowband images, which are captured in spectrally contiguous bands. The final product can therefore be considered a three-dimensional data cube (x, y, λ) in which the first two dimensions are the spatial dimensions, whereas the third dimension reflects the spectral dimension (Fig. 1). Thus many small bands of electromagnetic radiant energy are captured per pixel location. Just as a pixel of a common digital colour photograph contains three samples or Digital Numbers (DNs) at the same location to represent the amount of radiation captured in the three broad spectral bands, a hyperspectral image features N DNs, in which N equals the amount of spectral bands that are sampled. Every image is also characterised by a certain bit depth (e.g. integer 10-bit or values between 0 and 1023), which determines the resolution by which the at-sensor radiance L can be mapped onto a discrete set of digital values. From these DNs, reflectance (or emission) can be calculated. Through a combination of all these many

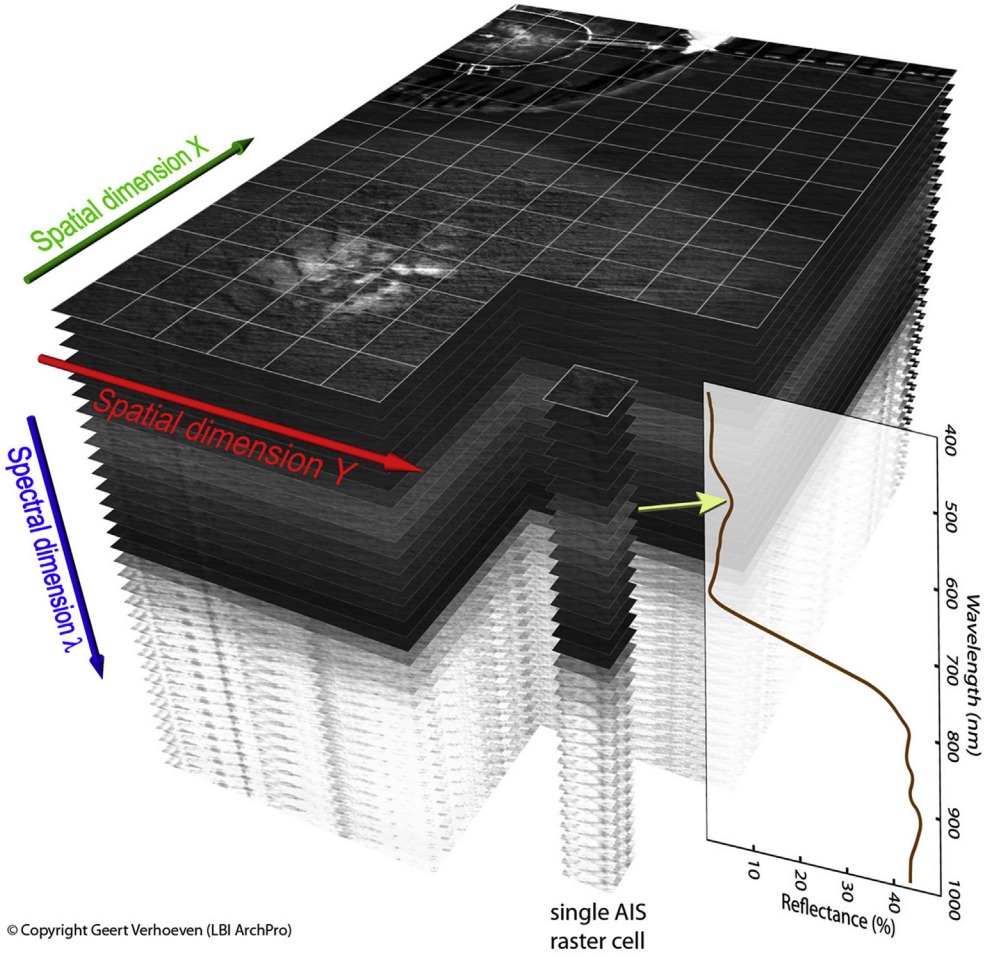

Fig. 1. Visualization of an AIS data cube.

single reflectance values, every individual pixel of the final image holds the complete reflectance or emission spectrum (known as spectral signature) of the material that was sampled at that specific location (Fig. 1). Since this spectral signature can be obtained for every pixel in the image, the technique is also (and more accurately) denoted Airborne Imaging Spectroscopy (AIS), spectroscopy being the study of interaction between radiant energy and matter.

2.3. AIS information extraction

Because imaging spectroscopy provides a spectrally continuous sampling of the objects that are imaged, it allows to assess specific and subtle vegetation characteristics (e.g. stressed versus healthy plants) and soil properties (e.g. mineral composition) to a much higher extent than any standard photographic or multispectral method. This is the reason why archaeological AIS has already several years ago been defined as a domain with "huge opportunities for the efficient detection, mapping and management of cultural heritage" (Traviglia, 2006b).

Despite the better spatial and spectral resolutions, working with AIS data necessitates expert knowledge and specialised software, which is again a limiting factor for its archaeological use. Assuming that the image geometry and georeferencing can be handled correctly, one needs to deal with the data quality and dimensional overload. Indeed, as the upwelling electromagnetic radiation is recorded in small spectral bands, the signal received by the sensor is quite low compared to sensor noise and possible atmospheric perturbations. The small instantaneous field of view (IFOV) of the AIS sensors – necessary for obtaining a sufficiently high spatial resolution – further limits the useful signal incident on the photodetectors. To deal with this low signal-to-noise ratio (SNR) as well as the huge amount of available information that is not directly accessible by the human visual system, data mining and intelligent pre- and post-processing approaches are necessary.

To date, researchers generally apply a few processing techniques such as Principal Component Analysis (PCA; Aqdus et al., 2008; Coren et al., 2005; Traviglia, 2006a) and various vegetation indices (Bennett et al., 2012; Cavalli et al., 2007; Emmolo et al., 2004; Traviglia, 2006b) to reduce the data complexity and extract archaeologically valid information.

In essence, PCA is a mathematical procedure that decreases the data redundancy by transforming a set of (possibly) correlated variables (original image data) into a new set of variables that are uncorrelated – the latter variables denoted the Principal Components (PCs). These PCs are linear combinations of the original variables (Liu and Mason, 2009) and are orthogonal to each other. The first principal component (i.e. the variable on the first axis) accounts for as much of the variability in the original data as possible, while every succeeding principal component contains decreasing amounts of variance in the remaining data. The first PC bands thus holds most image information, while the higher order bands are often only filled with noise, although they still might display very rare features (as also noted by Traviglia, 2006a). In remote sensing, PCA is often used since the newly calculated component images might reveal information that would go unnoticed in the original data.

Vegetation indices (or VIs) are arithmetic combinations of DNs, radiance or reflectance values in two or more spectral bands. Potentially, this combination highlights a specific feature of the vegetation while reducing the perturbing effects caused by solar geometry, atmosphere, topography, viewing angle and exposed soil. There exists a variety of VIs, each of them using different datasets and optimised for specific purposes (e.g. Bannari et al., 1995). As a result, they all have their strengths and weaknesses as well as operational scales. As such, not all these VIs are of archaeological benefit. Although disciplines such as precision farming might require specific VIs that deliver accurate estimates of crop yield and leaf chlorophyll content, archaeological air- and space-borne reconnaissance rather needs reliable, generally applicable methods that can be extended across entire landscapes, at different times of the day, and during various growing seasons (rather than very specific approaches that might vary from field to field, crop to crop, and by time of year – Verhoeven, 2012b).

Although both PCA and VIs have proven their success in some cases, more advanced processing procedures have to be exploited now that AIS data sets have the potential to even disclose very small archaeological features.

3. Case study and data acquisition

To test the potential of new AIS sensors and archaeologically-relevant image processing approaches, the Ludwig Boltzmann Institute for Archaeological Prospection and Virtual Archaeology (LBI ArchPro – Trinks et al., 2012) had set up a strategy, where three Austrian case study areas – Carnuntum, Kreuttal and St. Anna – have been surveyed repeatedly between 2010 and 2012. In the following, only data covering the area of Carnuntum, located approximately 40 km south-east of Vienna (N 48° 6′ 41″, E 16° 51′ 57″ – WGS84), was used.

Carnuntum is known as an important archaeological area, which is situated at the Roman limes on the southern bank of the Danube River (Fig. 2). It was an important focal point throughout the first four centuries AD and as such the capital of the former Roman province *Pannonia superior* (Jobst et al., 1983). The area is characterized by the river Danube and its gravel terraces. Buried under an intensively cultivated calcic chernozem (Neubauer et al., 2002), the archaeological remains covering an area of roughly 6.5 square kilometres usually produce well visible vegetation marks during the month of June. During the last decades, Carnuntum has been a focus for non-destructive archaeological prospection (Doneus et al., 2013; Neubauer et al., 2012, 2014; Saey et al., 2013; Seren et al., 2007). Specifically, since 2010 it has become a case-study area of the LBI ArchPro. As a result, a complete interpretation of the aerial archaeological evidence from 50 years of reconnaissance is available (Doneus et al., 2013).

Altogether, four scanning campaigns were realized by the Austrian LBI partner Airborne Technologies. All of the data were acquired in high spatial and spectral resolution with GSDs between 40 cm and 60 cm in 65–105 spectral bands between 400 nm and 1000 nm and digitised as 12-bit integer DNs (Table 1).

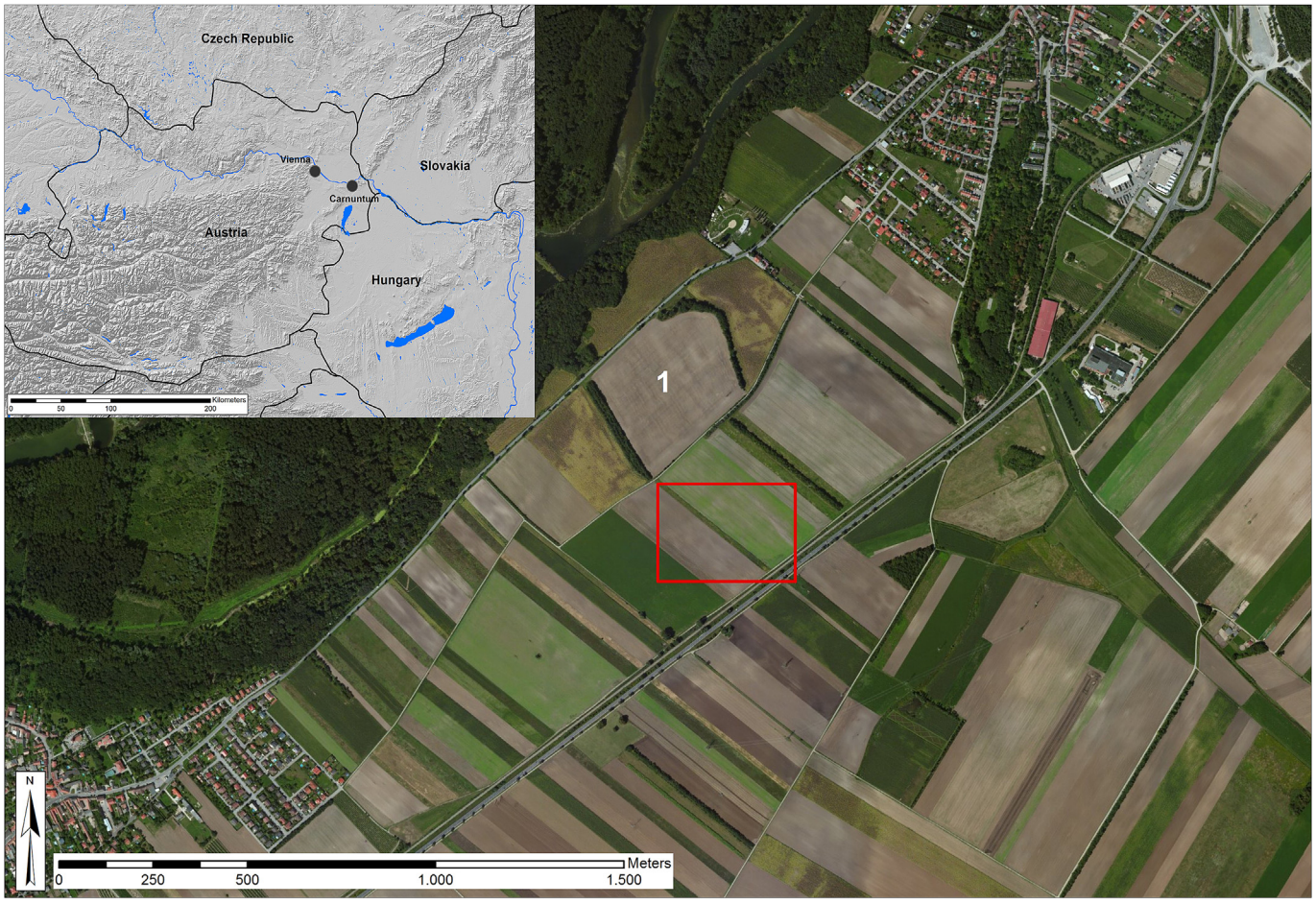

Fig. 2. The case study area of Carnuntum. 1: Legionary fortress; red rectangle: sample area described in the discussion below (see also Figs. 5 and 7). (For interpretation of the references to colour in this figure legend, the reader is referred to the web version of this article.)

Table 1
Flight parameters of the AIS data acquisition campaigns over the case study area of Carnuntum, Lower Austria. (FWHM means Full Width at Half Maximum).

Case study area	*Carnuntum*	*Carnuntum*	*Carnuntum*	*Carnuntum*
Date of data acquisition	5 June 2010	26 May 2011	11 November 2011	18 June 2012
Purpose of scan	Archaeology	Archaeology	Archaeology	Archaeology
Imaging spectrometer	AisaEAGLET (SPECIM)	AisaEAGLE (SPECIM)	AisaEAGLE (SPECIM)	AisaEAGLE (SPECIM)
Number of bands	105	65	65	65
Spectral sampling interval	5.3–5.9 nm	8.6–9.5 nm	8.6–9.5 nm	8.6–9.5 nm
Spectral resolution	3.3 nm at FWHM	3.3 nm at FWHM	3.3 nm at FWHM	3.3 nm at FWHM
Spectral range	400–1001 nm	403–995 nm	403–995 nm	403–995 nm
Binning	8	8	8	8
Flying height above ground	550/700 m	600 m	600 m	600 m
Ground Sampling Distance	0.4 m/0.6 m	0.4 m	0.4 m	0.4 m
Speed of aircraft	50 m/sec	50 m/sec	50 m/sec	50 m/sec
Digitisation	12-bit	12-bit	12-bit	12-bit

Simultaneously with the hyperspectral data acquisition (using an AISA Eaglet and AISA Eagle device), a full waveform laser scan (at least 10 points per m^2) using a RIEGL LMS-Q680i and vertical photographs (IGI-DigiCam H39 with a 50 mm lens) were acquired. The laser scan resulted in a high quality digital surface model (DSM), which was used for the orthorectification of both the hyperspectral scan and the vertical aerial photographs.

Both atmospheric correction and accurate georeferencing were necessary to combine the resulting multi temporal hyperspectral data and to integrate them with other prospection techniques applied by the LBI Archpro (mainly aerial photography, magnetics and ground-penetrating radar). This was achieved using the applications ATCOR for radiometric correction (only for AisaEAGLE data) and PARGE® (http://www.rese.ch) for accurate georeferencing with sub-pixel accuracy.

4. New ways of AIS information extraction using the ARCTIS toolbox

To analyse the corrected and orthorectified AIS data blocks, a MATLAB® toolbox called ARCTIS (ARChaeological Toolbox for Imaging Spectroscopy) with accompanying user-friendly Graphical User Interface (GUI) was developed (Atzberger et al., 2014; Atzberger and Wess, 2012). The toolbox allows the image analyst (not necessarily a specialist in remote sensing or imaging spectroscopy) to get a maximum of archaeological information out of the recorded 3D data cube. As the main focus for the toolbox is archaeological prospection, the aim was to visualize the data (or subsets of it) and extract possibly occurring vegetation and soil marks.

The toolbox allows to analyse small datasets providing all of the functions which have been identified in the past as useful for archaeological information extraction. In addition, several new functionalities were developed and integrated. In a first step the geometrically and radiometrically corrected data are imported and some further pre-processing is performed. To deal with the noise in the individual spectral bands (which is even more present when no radiometric correction is applied beforehand), a very powerful and commercially unavailable spectral smoothing filter (based on the Whittaker smoother – Atzberger and Eilers, 2011a, 2011b) was implemented in ARCTIS. After its executing, a very great deal of image noise is removed from all individual spectral bands without risking the removal of important spectral features or inducing new spectral artefacts.

For the subsequent information extraction (from now on simply denoted as processing), several tools have been compiled: PCA, a collection of the most important vegetation indices, a similarity function, edge-extraction techniques, and classification by k-means clustering. Due to the highly correlated nature of the spectral information in the individual bands of an AIS dataset and the omnipresent image noise, image processing techniques such as PCA or Minimum Noise Fraction (MNF) are often used to calculate a spectral subset of the initial data cube by rejecting the noisy components. The two new methods presented in the following paragraphs – red edge inflection point (REIP) and distribution fitting – take, however, the complete AIS dataset into account: REIP describes the spectral shape of the reflectance curve whereas the distribution fitting parameterizes the shape of the frequency distribution of the reflectance values.

4.1. Red edge inflection point

In the first method, called the Red Edge Inflection Point (REIP), specific attention is given to the Red Edge. This Red Edge is a transition zone around 700 nm in the visible far-Red to NIR transition spectrum, for healthy vegetation characterized by a steep slope of the spectral reflectance curve (Fig. 3A). This very abrupt reflectance change results from the fact that the absorption by chlorophyll pigments in the far-Red spectrum (around 670–680 nm) is high and the NIR reflection by the spongy mesophyll is high, giving rise to one of the most extreme slopes to be found in reflectance spectra of natural materials. When vegetation gets stressed, this Red Edge shifts toward shorter wavelengths due to the stress related increase of reflectance at wavelengths near 700 nm (Fig. 3A). This “Blue shift” of the Red Edge is currently accepted as the most consistent stress response of plants to different stressors (Boochs et al., 1990; Gitelson et al., 1996; Horler et al., 1983). Previous research has already proven the archaeological usefulness of the red edge spectral band when used in a simple vegetation index (Bennett et al., 2012; Verhoeven, 2009; Verhoeven and Doneus, 2011; Cho et al., 2008; Darvishzadeh et al., 2009). Since AIS sensors often sample the Red Edge in a few bands, it is one of the first spectral regions one should focus on when looking for vegetation stress in the complete optical region (Carter et al., 2002).

The REIP algorithm in ARCTIS will use the complete red edge spectrum to look for its inflection point (as is marked by a red cross in the spectral curve in Fig. 3B). To this end, the user first defines the region he wants the algorithm to focus on. For the REIP, often the 680 nm–760 nm region is chosen. However, this freedom of choice indicates that one is not limited to the red edge. Although not denoted REIP anymore, inflection points might also be estimated in the short-wavelength infrared or the green waveband. This inflection point is the location of the highest gradient in the spectral profile of the predetermined spectral range.

In ARCTIS, some pre-processing steps can be performed to obtain more accurate results (Fig. 3B) (Atzberger et al., 2014). To start, the Whittaker smoother can be applied during the call of the

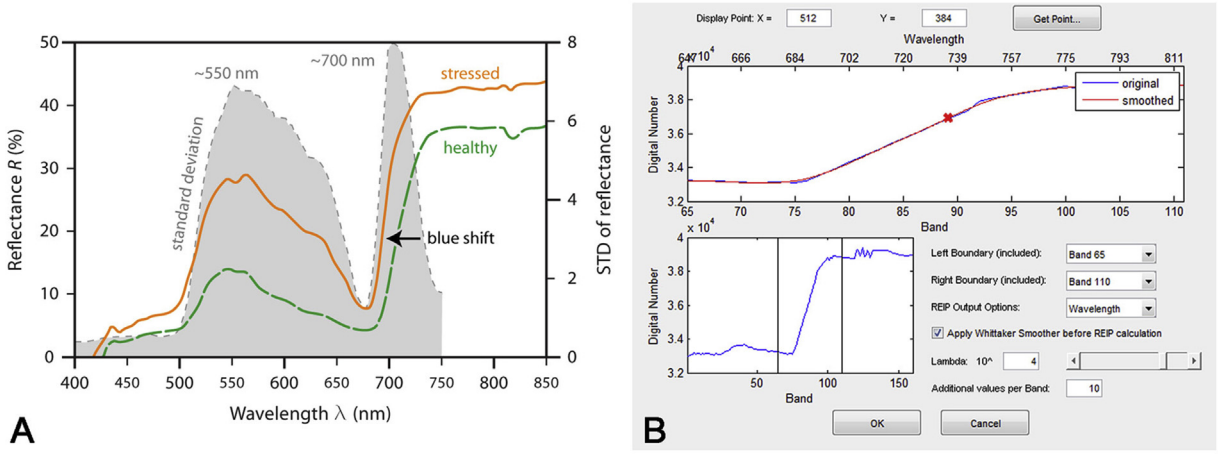

Fig. 3. (A) Typical reflectance responses of a *Radiata* pine leaf. The discontinuous green curve represents the mean reflectance for healthy, chlorophyll-rich leaves, while the upper orange curve indicates the mean reflectance for a stress situation (nitrogen deficiency). The grey curve represents the standard deviation of reflectance calculated from reflectance spectra of maize leaves with varying chlorophyll content (Verhoeven and Doneus, 2011, Fig. 1A). (B) The Red Edge Inflection Point GUI as it is currently implemented in the ARCTIS toolbox (see text for more details on the available functionality). The red cross marks the position of the inflection point. (For interpretation of the references to colour in this figure legend, the reader is referred to the web version of this article.)

REIP algorithm, where each AIS pixel is smoothed independently along the *z*-axis (i.e. spectral dimension) according to a user-defined smoothing parameter lambda (λ). Additionally, the smoothed input AIS data can be spectrally interpolated to a user-defined number of fictional bands between the original spectral bands leading to a finer spectral resolution of the detected REIP location (Fig. 3B). Whatever pre-processing steps were chosen, the REIP is finally calculated on a pixel-by-pixel basis, where for each pixel the inflection point is located, i.e. the steepest slope of the smoothed and interpolated spectral curve within the predefined spectral region. From each inflection point, three parameters can be derived, which can be compiled into three new image layers:

- Layer 1: band or wavelength of the REIP location;
- Layer 2: value of the slope of the reflectance curve at the REIP position;
- Layer 3: reflectance value or DN at REIP.

4.2. Distribution fitting

A second technique embedded in ARCTIS is called distribution fitting, for which an algorithm tries to fit a user-defined function to the frequency distribution of a pixel's spectral values (Atzberger et al., 2014). Fig. 4 depicts this process. First, the algorithm retrieves all the spectral data from one hyperspectral pixel. The latter consists of various reflectance values: one for each of the acquired spectral bands. Since these data are univariate (i.e. they provide information on one variable, being reflectance) a frequency histogram can be calculated. Fig. 4 shows the histograms and spectral signatures of two completely different AIS pixels: one pixel stores the reflectance values from a healthy green, chlorophyll-rich leaf, while the other pixel digitised the reflectance of a stressed, yellow leaf. From the spectral reflectance curve, it is obvious that the stressed leaf suffered from a severe loss of Chlorophyll pigments. First of all, the Green reflectance peak around 550 nm is broadened towards longer wavelengths and causes the leaf to appear yellowish (a phenomenon called chlorosis – Adams et al., 1999). At the same time, the Red Edge shifts toward shorter wavelengths due to the stress related increase of reflectance at wavelengths near 700 nm (i.e. the Blue shift). The shape of the spectral curves is also directly influencing their corresponding histogram. Consider for example the reflectance in the 25%–30% interval. From the spectral curve, one can infer that the healthy green leaf has only one band (band number 53 in the red edge region) with a reflectance value in this range, which leads to a single count in this bin. This contrasts highly with the chlorotic leaf pixel, which consists of almost twenty bands (i.e. bands 30–50) with a reflectance value in this range. As a result, the histogram bin for this reflectance range has a height of eighteen counts. This relationship between the reflectance curve and its histogram now clarifies the more homogenous frequency distribution in the chlorotic histogram with only one large NIR peak, whereas the healthy leaf histogram is dominated by two large peaks that are related to the low reflectance in the visible range and the high NIR reflectance respectively.

After building the frequency distribution histogram for one AIS pixel, a predefined Probability Density Function (PDF) f is fitted to it. In probability theory, various PDFs are used to mathematically describe the specific distribution of a random variable (the reflectance in this case). Since random variables can be continuous or discrete, both types of PDFs exist as well. In the continuous category, many different PDFs reside: normal or Gaussian, Rayleigh, exponential, Weibull, beta, gamma, chi, Student's t-distribution etc. The Poisson and Boltzmann density functions are both examples of the discrete class. Any of these PDFs is defined by its parameters. The normal density function describing the normal distribution, for instance, is parameterized in terms of a mean parameter μ and a standard deviation σ (Moore and McCabe, 2003). In ARCTIS, a number of discrete and continuous theoretical PDFs reside and all can be parameterized.

Thus, after generating the histogram from the acquired signal (i.e. the pixel's values), the algorithm will parameterise the chosen PDF so that it best characterizes this pixel-specific histogram. The values of the parameters describing this PDF will then make up the DNs of the newly generated image; the number of image layers will equal the number of parameters of the PDF. Fig. 4 shows the results one gets with two different PDFs: the normal and the gamma continuous density functions. Since both PDFs are mathematically different, they will obviously yield dissimilar results for the same histogram. Besides, different histograms will yield dissimilar parameters for the same PDF. So, in the case of the green leaf, a new two-band image will be created with pixel values 31 and 21 when

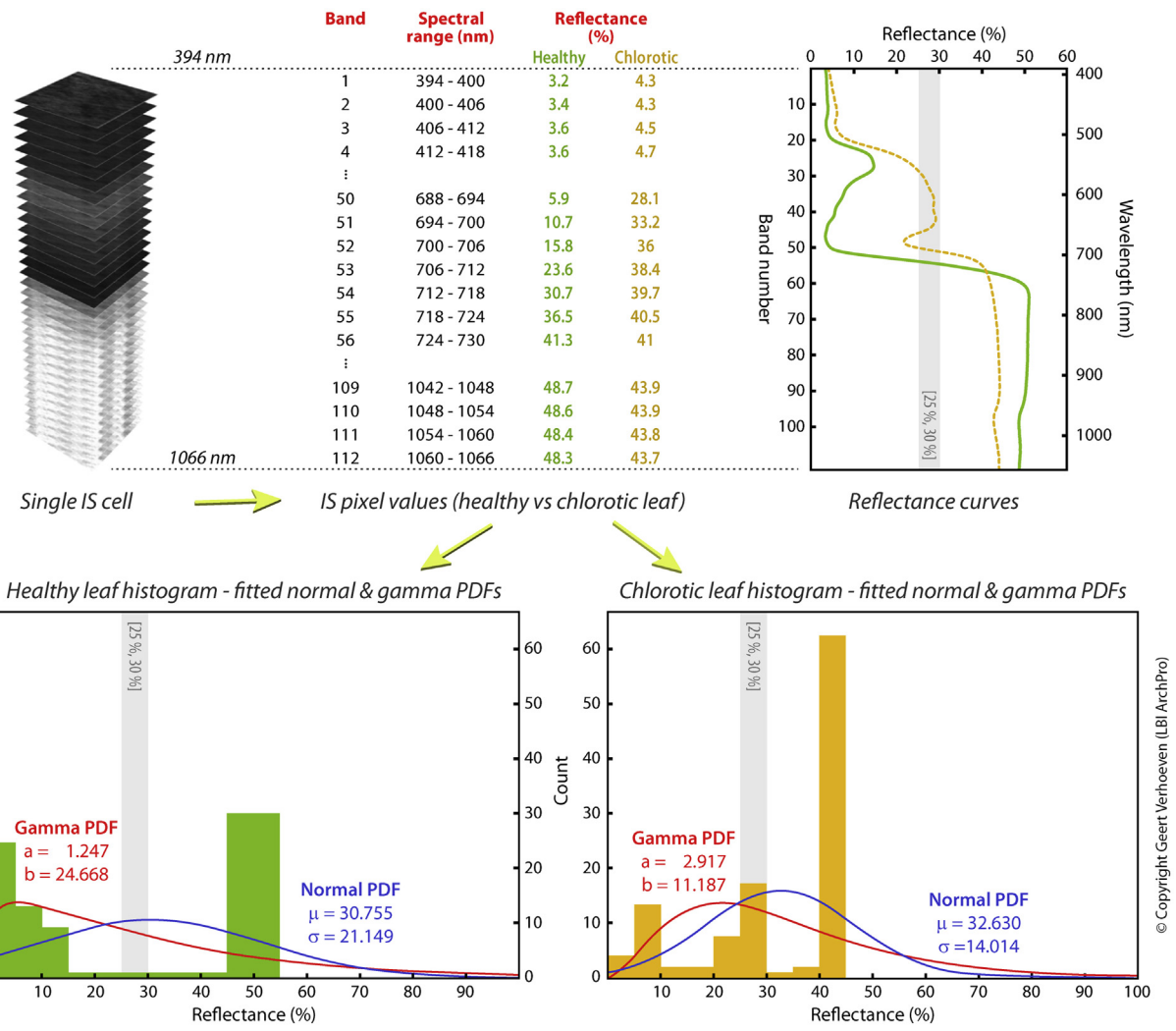

Fig. 4. The principle of a pixel-wise distribution fitting (more information provided in the text).

choosing the normal PDF. This process is then repeated for each pixel of the AIS data block. When the neighbouring pixel of the original AIS image holds for instance the reflectance spectrum of the chlorotic leaf, the new pixel values will become 33 and 14.

The result of this very computing intensive process is a two-band image, in which the difference between stressed and healthy vegetation is visualised in a completely new manner. The exact amount of image channels that are computed completely depends on the PDF selected. Obviously, in the case one would pick a PDF that is parameterised by three values, a three-band image is produced. Initial promising results obtained with this new technique were briefly reported by Verhoeven et al. (2013), but here the coverage will be more in depth.

After testing a handful of functions, the gamma and normal continuous density functions yielded the best results on our dataset. This is due to the fact that the gamma density function can cope very well with the right skewed histograms from healthy vegetation, which makes its parameterisation completely different when dealing with stressed vegetation histograms (see Fig. 4). Although the gamma density function is often parameterized with a shape parameter k and scale parameter θ, ARCTIS uses the parameterization embedded in MATLAB®, which is based on a shape parameter a ($= k$) and a rate parameter b ($= 1/\theta$) (The MathWorks, 2013). The Normal density function is parameterized in terms of a mean parameter μ and a standard deviation σ (Moore and McCabe, 2003). Since MATLAB produces two additional values, being the lower and upper bound of the confidence interval for μ (The MathWorks, 2014), the results is a four band image. One does, however, not have to use all four generated bands and can only focus on one band (i.e. a greyscale image) or on two or three bands (i.e. a false-colour image). Since the mean μ of the normal PDF is often not very dissimilar for stressed versus healthy vegetation fittings (see Fig. 4), its standard deviation σ often displays the contrast best (see also next section and Fig. 5C).

5. Results

For the following discussion, a sample area was chosen within the former *canabae legionis* south-west of the Roman legionary fortress (see red rectangle in Fig. 2). It contains several fields with different crops.

Fig. 5 clearly indicates the remarkable enhancement one can obtain through REIP processing and distribution fitting. Data acquisition was on May 26 2011, which was due to wet conditions during April at the beginning of the "vegetation-mark season", when differences in height and colour of the vegetation started to emerge. According to Metop/ASCAT soil moisture data viewer (ASCAT, 2014) the degree of saturation of the soil moisture content of the upper soil layer (<2 cm) was 12.55%.

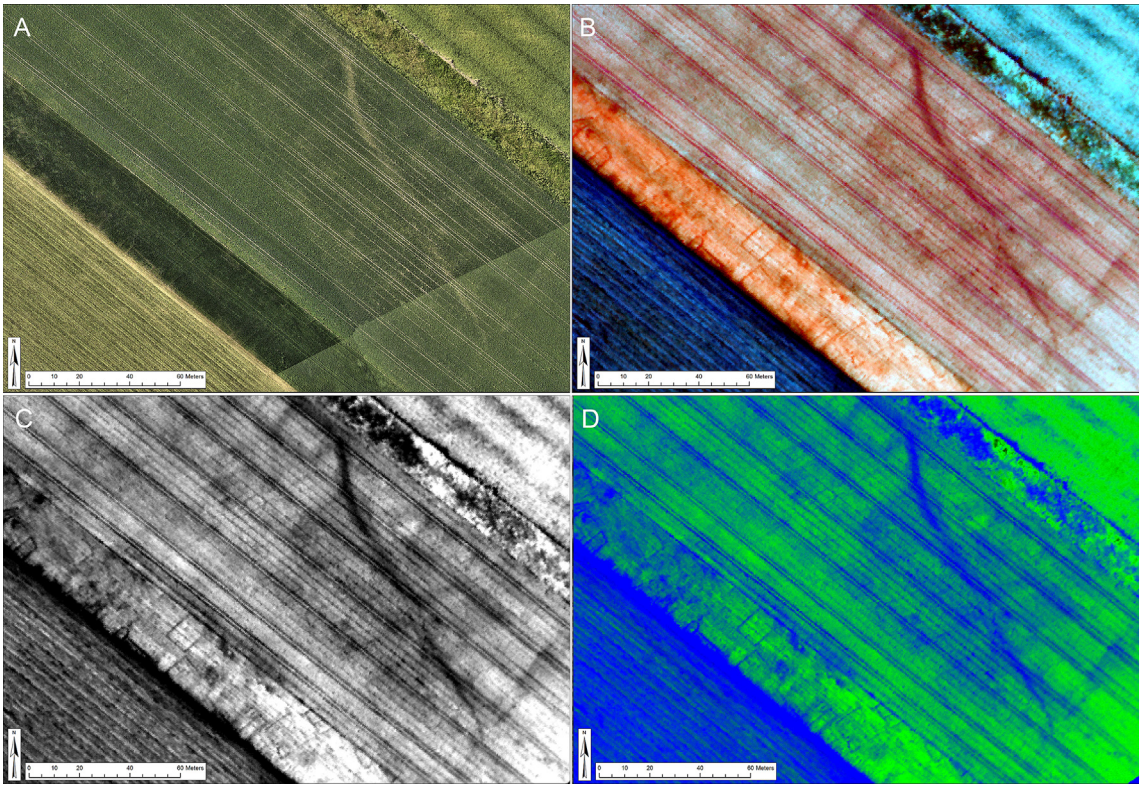

Fig. 5. Data from Carnuntum, Lower Austria, acquired on May 26 2011. (A) Conventional orthorectified aerial image, acquired in the visible spectrum. GSD of 0.1 m; enhanced using contrast limited adaptive histogram equalization (*CLAHE*); (B) false colour composite created by means of the REIP algorithm (R = band 1 (wavelength), G = band 2 (slope), B = band 3 (reflectance value)). (C) rate parameter *b* of the gamma distribution fitting; (D) normal distribution fitting (R = NONE, G = band 2 (σ), B = band 1 (μ)). GSDs of (B), (C) and (D): 0.4 m. Figures B, C, and D were subject to the same histogram stretch by means of standard deviation. (For interpretation of the references to colour in this figure legend, the reader is referred to the web version of this article.)

To improve the visibility of archaeological traces captured in the conventional aerial photograph, a contrast limited adaptive histogram equalization (*CLAHE* — Zuiderveld, 1994) was applied (Fig. 5A). Still the photograph displays only very few marks, which are almost entirely located in the narrow dark-green field extending from the upper left corner towards the middle of the lower edge. They can be described as negative vegetation marks, which are a consequence of (in this case) buried walls of Roman buildings. In the large field to the right, a Roman road is revealed by a linear arrangement of yellow (i.e. already stressed) crops (Fig. 6A).

The false colour composite created by means of the REIP algorithm (R = wavelength, G = slope, B = reflectance value) is displayed in Fig. 5B. It enhances the differences in plant physiology and consequently allows the archaeological features to be seen more clearly. Especially the above mentioned negative vegetation marks in the narrow field can now be read in detail, while further archaeologically induced traces become visible in the larger field to the right. Their contrast is fainter, but they can be identified as remains of buried buildings located on both sides of the Roman road, which is now clearly visible in dark red (Fig. 6B).

The results of fitted gamma (Fig. 5C) and normal (Fig. 5D) PDFs perform almost equally well. For the gamma distribution fitting, the histogram-stretched version of the rate parameter *b* gave the best results, while a combination of the standard deviation σ (band 2) and the upper bound of the confidence interval for μ (band 4) (R = band 4, G = band 2, B = band 2) turned out to be the best combination to identify vegetation marks in this scene. The explanation for this can be deduced from the spectral signatures in Fig. 4, as they are very similar to the spectral reflectance curves of the chlorotic and green vegetation in these fields. Both fittings clearly indicate negative vegetation marks in darker tones. Although vegetation marks seem to be slightly enhanced in the PDF images, in terms of archaeological features there is virtually no difference to the REIP image (Fig. 6C and D compared to Fig. 6B). Slight variations do occur, where for each visualization other details have better visibility.

The situation is, however, different, when the season gets warmer and drier. Fig. 7 shows the slightly larger and shifted area of Fig. 5 as recorded on June 18, 2012, after a rather dry spring (ZAMG, 2014). The relative dry conditions are also reflected in the soil moisture data (ASCAT, 2014), which were relatively low during April and May and display around 14% saturation of the soil moisture content of the upper soil layer (<2 cm) at the date of data acquisition.

Both visualizations of the REIP image and gamma PDF have the same band combinations as in Fig. 5. For the normal PDF the standard deviation σ was chosen as the best visualization in this case (Fig. 7D). In the lower left part of the image, the Roman road from Fig. 5 is again visible, but due to a different crop (maize), no traces of the buildings can be seen in any of the visualizations. The two fields (annotations 1 and 2 in Fig. 7A) to the west do show detailed negative vegetation marks. Due to a soil moisture deficit, the summer crop in field 1 shows a yellow on green contrast between stressed and healthy plants, which is extremely well visible in the conventional photograph (Fig. 7A). This situation is more or less similar to the one displayed in Fig. 5, although slightly more pronounced in this case. Field 2 is grown with winter crop, which has already entirely ripened. Negative vegetation marks show in a darker brown colour, which makes a (less well visible) contrast to the surrounding yellow plants.

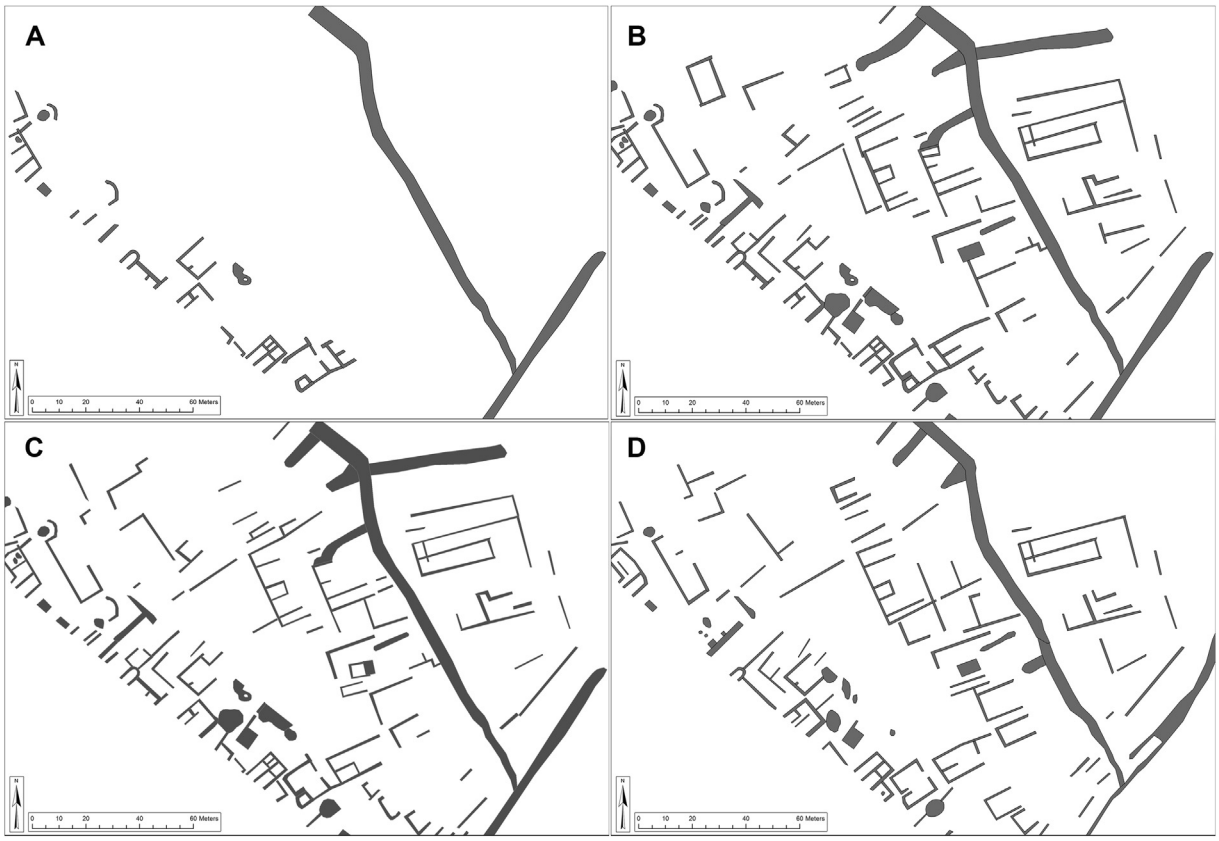

Fig. 6. Mapping of visualizations from Fig. 5: (A) orthophotograph, (B) REIP, (C) gamma distribution fitting, (D) normal distribution fitting.

In this situation, when vegetation marks become clearly evident in the visible part of the electromagnetic spectrum, the false colour image produced by the REIP algorithm cannot add or enhance archaeological information: while vegetation marks in field 1 are slightly less well visible (which is mainly due to the four times lower spatial resolution), calculation of the REIP is not successful at all in the already ripened vegetation of field 2 (Fig. 8B). This confirms what was already indicated in previous research: taking the Red edge into account is only very beneficial when one wants to identify and enhance weak vegetation stresses that are lost when taking only the broad visible spectrum into account (Verhoeven, 2009; Verhoeven and Doneus, 2011). When vegetation is imaged at the very end of the season and all plants are senescing, the red edge has completely disappeared. As a result, the REIP approach uses its edge over the visible and pure NIR frames. Both gamma (Fig. 8C) and normal (Fig. 8D) distribution function show better results than the REIP algorithm, but also cannot outperform the conventional photograph during this part of the growing season.

6. Discussion

These two examples show that airborne hyperspectral scanning can reveal detailed archaeological information, if a high-resolution data acquisition with a GSD below 1 m is available. At times when the vegetation mark season is at its beginning, or in a rather wet growing season (as was the case in 2011 – see Fig. 5) hyperspectral data may even outperform conventional aerial photography. A high spatial resolution will, however, increase the noise in the individual spectral bands, which needs sophisticated preparation of the data cube. In our case the Whittaker smoother, a very powerful spectral smoothing filter, was applied (for examples with and without smoothing, please consult Atzberger et al., 2014).

Both introduced methods of information extraction – REIP and distribution fitting – are useful add-ons to PCA and vegetation indices, which are the currently used techniques for reduction of data complexity and extraction of archaeological information. For the sake of this paper, mappings of all visualizations (Figs. 6 and 8) were added to demonstrate the archaeological information content of each method. A detailed assessment of the qualitative and quantitative performance of all these different methods as well as a comparison with other techniques (e.g. vegetation indices or PCA) will be however subject of another paper. Also further systematic testing in different environments and different archaeological site types will be necessary.

The results of the REIP and distribution fittings (as is also the case with PCA) are new bands, which are displayed by the imaging software (in our case ArcGIS) as false-colour colour or greyscale images. Depending on the situation of the data acquisition (land cover, date and time of data acquisition etc.) and the purpose and method of interpretation, different assignments of the resulting bands with one of the three image-channels will be necessary. This can be seen in this paper with the normal distribution fitting, where in Fig. 5D the assignment of channels G and B with bands 1 and 2 resulted in the best readability of vegetation marks, while in Fig. 7D the use of a single channel (band 2) seemed to be most appropriate.

To enable other colleagues to use the approaches discussed in this paper, ARCTIS will be released under creative commons licence free of charge via website (http://luftbildarchiv.univie.ac.at). While ARCTIS provides a large bundle of functions for archaeological

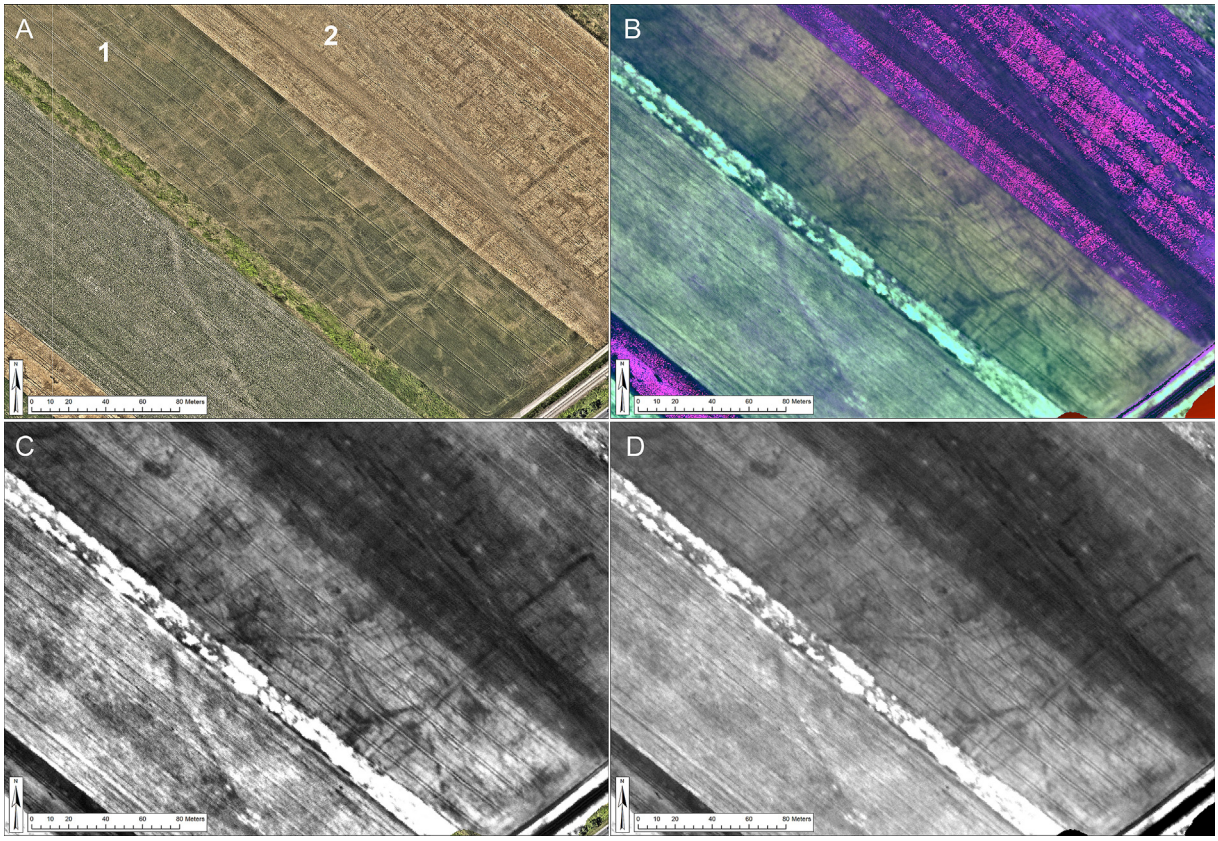

Fig. 7. Data from Carnuntum, Lower Austria, acquired on June 18 2012. (A) Conventional orthorectified aerial image, acquired in the visible spectrum. GSD of 0.1 m; enhanced using contrast limited adaptive histogram equalization (*CLAHE*). (B) false colour composite created by means of the REIP algorithm (R = band 1 (wavelength), G = band 2 (slope), B = band 3(reflectance value)). (C) rate parameter b of the fitted gamma PDF; (D) the standard deviation σ of the fitted normal PDF. GSDs of (B), (C) and (D): 0.4 m. Figures B, C, and D were subject to the same histogram stretch by means of standard deviation. (For interpretation of the references to colour in this figure legend, the reader is referred to the web version of this article.)

information extraction, it is not meant to be a competitor for professional commercial software packages. More than anything else, this toolbox and its residing algorithms must be considered a prototyping and testing environment. It is well known that the MATLAB® programming language focuses more on the ease of code development than on the performance found in languages such as C, C++ and Fortran. This characteristic becomes very apparent when executing the distribution fitting approach. Since all operations are executed on a pixel-by-pixel basis, the whole operation becomes very time-consuming in a MATLAB®-driven environment, which in turn restrains it from numerous test runs on large datasets. Although ARCTIS was initially developed to mine archaeological AIS data cubes, its current state prevents it from processing big datasets. In near future, when several AIS datasets have been processed and the outcome of specific processing workflows was validated by different practitioners, those specific algorithms (or combinations of them) that proved most useful will be implemented in C or C++ for faster execution, while the MATLAB® GUI can still be used to call these external programs.

Finally, archaeologists also need to find better ways to quantifying the gain of image processing algorithms. To date, the common practise in comparing different versions of one image (or different datasets) is by subjective, qualitative means. Science and the communication of results often ask for more objective, quantitative measures of possible gains. In addition to the development of new AIS processing algorithms and contrast enhancement techniques for all optical airborne imagery, the authors are currently working on new approaches to more robustly express the added value of these methods. The final aim of these attempts is to maximise the information extraction of remotely sensed archaeological footage, but also limit the AIS processing toolbox to a more confined set of approaches that generally deliver the biggest gains for extracting and interpreting archaeological features.

7. Conclusion and prospect

This study has investigated new approaches for analysing archaeological airborne imaging spectroscopy data: the red edge inflection point (REIP) and distribution fittings. REIP extracts information about plant vigour from the steep sloping spectral reflectance curve around 700 nm (transition from the visible far-Red to NIR spectrum). Finding the location of the highest gradient in the Red Edge spectral profile for each pixel, the algorithm generates a three band image (wavelength, slope, and reflectance). The distribution fitting will for each pixel fit a given PDF to the frequency histogram of its spectral signature and report the fitted parameters.

Both algorithms were programmed into a specific free of charge MATLAB® toolbox called ARCTIS, which was created to test currently available AIS processing practices as well as validate the value of completely new information extraction techniques. Two different high-resolution datasets, collected over the same area (the Roman town of *Carnuntum*, Austria) within two years showing different ground conditions were used to test the algorithms. The imagery under study has a ground-sampling distance of 40 cm, which allowed extraction of archaeologically relevant features in detail.

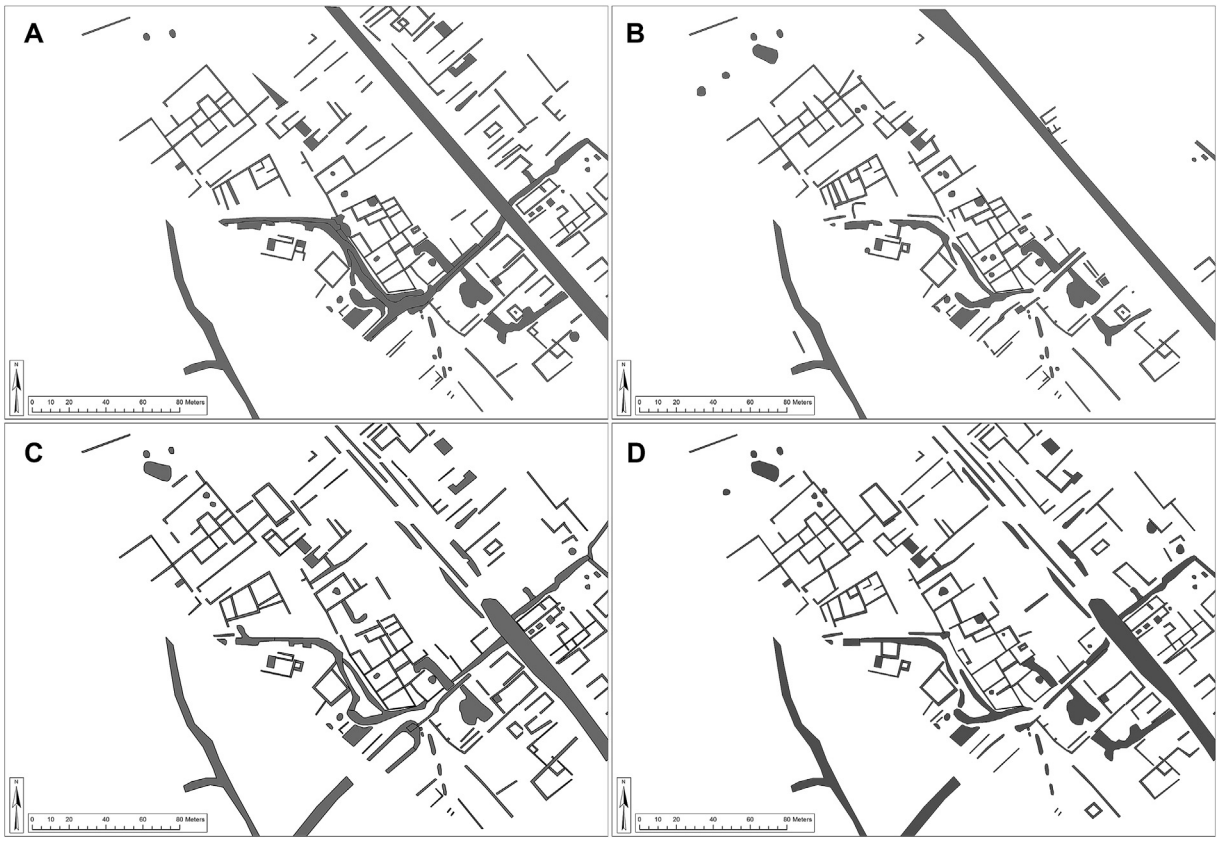

Fig. 8. Mapping of visualizations from Fig. 7: (A) orthophotograph, (B) REIP, (C) gamma distribution fitting, (D) normal distribution fitting.

The examples given here prove that, when compared to simultaneously acquired broadband visible imagery at a spatial resolution of 10 cm, distribution fitting and the REIP visualisations can increase the contrast between vigorous and stressed plants. That is, however, when the data are acquired at a high spatial resolution and at the correct moment in the plant's phenological cycle. Once the vegetation marks are also visibly very discernable, the specific advantages of both methods are seriously reduced and the vertical photographs show most of the archaeological information in very high detail.

Acknowledgements

The authors want to thank Agata Lugmayr for the radiometric correction and orthorectification of the used AIS datasets.

The Ludwig Boltzmann Institute for Archaeological Prospection and Virtual Archaeology (archpro.lbg.ac.at) is based on an international cooperation of the Ludwig Boltzmann Gesellschaft (A), the University of Vienna (A), the Vienna University of Technology (A), the Austrian Central Institute for Meteorology and Geodynamic (A), the office of the provincial government of Lower Austria (A), Airborne Technologies GmbH (A), 7Reasons (A), RGZM-Romano-Germanic Central Museum Mainz (D), RAÄ-Swedish National Heritage Board (S), IBM VISTA-University of Birmingham (GB), NIKU-Norwegian Institute for Cultural Heritage Research (N), and Vestfold County Council (N).

References

Adams, M.L., Philpot, W.D., Norvell, W.A., 1999. Yellowness index: an application of spectral second derivatives to estimate chlorosis of leaves in stressed vegetation. Int. J. Remote Sens. 20 (18), 3663–3675.

Aqdus, S.A., Drummond, J., Hanson, W.S., 2008. Discovering archaeological cropmarks: a hyperspectral approach. In: Proceedings of the XXIst ISPRS Congress, Technical Commission V, Beijing, China. 3–11 July 2008. ISPRS, pp. 361–365.

Aqdus, S.A., Hanson, W.S., Drummond, J., 2007. Finding archaeological cropmarks: a hyperspectral approach. In: Remote Sensing for Environmental Monitoring, GIS Applications, and Geology VII, Florence, Italy. 17 September 2007, 674908–674908-11.

Aqdus, S.A., Hanson, W.S., Drummond, J., 2012. The potential of hyperspectral and multi-spectral imagery to enhance archaeological cropmark detection: a comparative study. JAS 39 (7), 1915–1924.

ASCAT, 2014. http://rs.geo.tuwien.ac.at/dv/ascat/ (last accessed: 24.06.14.).

Atzberger, C., Eilers, P.H.C., 2011a. A time series for monitoring vegetation activity and phenology at 10-daily time steps covering large parts of South America. Int. J. Digit. Earth 4 (5), 365–386.

Atzberger, C., Eilers, P.H.C., 2011b. Evaluating the effectiveness of smoothing algorithms in the absence of ground reference measurements. Int. J. Remote Sens. 32 (13), 3689–3709.

Atzberger, C., Wess, M., 2012. Crop Mark Documentation. Universität für Bodenkultur, Wien, p. 60.

Atzberger, C., Wess, M., Doneus, M., Verhoeven, G.J.J., 2014. ARCTIS – a MATLAB® toolbox for archaeological imaging spectroscopy. Remote Sens. 6, doi:10.3390/rs60x000x (in print).

Bannari, A., Morin, D., Bonn, F., Huete, A.R., 1995. A review of vegetation indices. Remote Sens. Rev. 13 (1–2), 95–120.

Barnes, I., 2003. Aerial remote-sensing techniques used in the management of archaeological monuments on the British Army's salisbury plain training area, Wiltshire, UK. Archaeol. Prospect. 10 (2), 83–90.

Bassani, C., Cavalli, R.M., Fasulli, L., Palombo, A., Pascucci, S., Santini, F., Pignatti, S., 2009a. Integration of airborne optical and thermal imagery for archaeological subsurface structures detection: the Arpi case study (Italy). Geophys. Res. Abstr. 11, 7717.

Bassani, C., Cavalli, R.M., Goffredo, R., Palombo, A., Pascucci, S., Pignatti, S., 2009b. Specific spectral bands for different land cover contexts to improve the efficiency of remote sensing archaeological prospection: the Arpi case study. J. Cult. Herit. 10, e41.

Bennett, R., Welham, K., Hill, R.A., Ford, A.L.J., 2012. The application of vegetation indices for the prospection of archaeological features in grass-dominated environments. Archaeol. Prospect. 19 (3), 209–218.

Bennett, R., Welham, K., Hill, R.A., Ford, A.L.J., 2013. Airborne spectral imagery for archaeological prospection in grassland environments—an evaluation of performance. Antiquity 87 (335), 220–236.

Boochs, F., Kupfer, G., Dockter, K., Kühbauch, W., 1990. Shape of the red edge as vitality indicator for plants. Int. J. Remote Sens. 11 (10), 1741–1753.
Carter, G.A., 1994. Ratios of leaf reflectances in narrow wavebands as indicators of plant stress. Int. J. Remote Sens. 15 (3), 697–703.
Carter, G.A., Estep, L., Muttiah, R.S., 2002. General spectral characteristics of leaf reflectance responses to plant stress and their manifestation at the landscape scale. In: Muttiah, R.S. (Ed.), From Laboratory Spectroscopy to Remotely Sensed Spectra of Terrestrial Ecosystems. Kluwer Academic Publishers, Dordrecht, pp. 271–293.
Cavalli, R.M., 2013. Integrated approach for archaeological prospection exploiting airborne hyperspectral remote sensing. In: Corsi, C., Slapšak, B., Vermeulen, F. (Eds.), Good Practice in Archaeological Diagnostics. Non-invasive Survey of Complex Archaeological Sites. Natural Science in Archaeology. Springer International Publishing, Cham, pp. 87–112.
Cavalli, R.M., Colosi, F., Palombo, A., Pignatti, S., Poscolieri, M., 2007. Remote hyperspectral imagery as a support to archaeological prospection. J. Cult. Herit. 8 (3), 272–283.
Cavalli, R.M., Licciardi, G.A., Chanussot, J., 2012. Detection of anomalies produced by buried archaeological structures using nonlinear principal component analysis applied to airborne hyperspectral image. IEEE J. Sel. Top. Appl. Earth Obs. Remote Sens. 5 (6), 1–12.
Cavalli, R.M., Pignatti, S., 2001. Il telerilevamento iperspettrale da aereo per lo studio dei beni archeologici: applicazione dei dati iperspettrali MIVIS. In: Campana, S., Forte, M. (Eds.), Remote sensing in archaeology. XI Ciclo di lezioni sulla ricerca applicata in archeologia, Certosa di Pontignano (Siena), 6–11 dicembre 1999. All'insegna del giglio, Firenze, pp. 221–232.
Challis, K., Kincey, M., Howard, A.J., 2009. Airborne remote sensing of valley floor geoarchaeology using Daedalus ATM and CASI. Archaeol. Prospect. 16 (1), 17–33.
Cho, M.A., Skidmore, A.K., Atzberger, C., 2008. Towards red-edge positions less sensitive to canopy biophysical parameters for leaf chlorophyll estimation using properties optique spectrales des feuilles (PROSPECT) and scattering by arbitrarily inclined leaves (SAILH) simulated data. Int. J. Remote Sens. 29 (8), 2241–2255.
Coleman, S., 2007. Taking advantage: vertical aerial photographs commissioned for local authorities. In: Mills, J., Palmer, R. (Eds.), Populating Clay Landscapes. Tempus, Stroud, pp. 28–33.
Coren, F., Visintini, D., Prearo, G., Sterzai, P., 2005. Integrating LiDAR intensity measures and hyperspectral data for extracting of cultural heritage. In: Workshop Italy-Canada 2005, Padova, Italy. 17–18 Maggio 2005.
Crawshaw, A., 1995. Oblique aerial photography – aircraft, cameras and films. In: Kunow, J. (Ed.), Luftbildarchäologie in Ost- und Mitteleuropa/Aerial Archaeoloy in Eastern and Central Europe. Internationales Symposium 26.–30. September 1994 Kleinmachnow, Land Brandenburg, Forschungen zur Archäologie im Land Brandenburg, vol. 3. Verlag Brandenburgisches Landesmuseum für Ur- und Frühgeschichte, Potsdam, pp. 67–76.
Darvishzadeh, R., Atzberger, C., Skidmore, A.K., Abkar, A.A., 2009. Leaf area index derivation from hyperspectral vegetation indices and the red edge position. Int. J. Remote Sens. 30 (23), 6199–6218.
Doneus, M., 1997. On the archaeological use of vertical photographs. AARG News 15, 23–27.
Doneus, M., Gugl, C., Doneus, N., 2013. Die Canabae von Carnuntum: Eine Modellstudie der Erforschung römischer Lagervorstädte: von der Luftbildprospektion zur siedlungsarchäologischen Synthese. Österreichische Akademie der Wissenschaften, Wien, p. 296.
Emmolo, D., Franco, V., Lo Brutto, M., Orlando, P., Villa, B., 2004. Hyperspectral techniques and GIS for archaeological investigation. In: Proceedings of ISPRS 2004-geo-imagery Bridging Continents. XXth ISPRS Congress, Istanbul, Turkey. 12–23 July 2004. ISPRS, Istanbul.
Forte, E., Pipan, M., Sugan, M., 2011. Integrated geophysical study of archaeological sites in the aquileia area. In: Proceedings of the 1st Workshop on the New Technologies for Aquileia (NTA-2011), Aquileia, Italy. May 2, 2011. Department of Mathematics and Computer Science, University of Udine.
Gitelson, A.A., Merzlyak, M.N., Lichtenthaler, H.K., 1996. Detection of red edge position and chlorophyll content by reflectance measurements near 700 nm. J. Plant Physiol. 148 (3–4), 501–508.
Hampton, J.N., 1974. An experiment in multispectral air photography for archaeological research. Photogramm. Rec. 8 (43), 37–64.
Hanson, W.S., 2008. The future of aerial archaeology (or are algorithms the answer?). In: Remote Sensing for Archaeology and Cultural Heritage Management. Proceedings of the 1st International EARSeL Workshop, CNR, Rome. September 30-October 4, 2008. Arracne, Rome, pp. 47–50.
Horler, D.N.H., Dockray, M., Barber, J., 1983. The red edge of plant leaf reflectance. Int. J. Remote Sens. 4 (2), 273–288.
Jobst, W., Stiglitz, H., Kandler, M., 1983. Provinzhauptstadt Carnuntum: Österreichs grösste archäologische Landschaft. Österreichischer Bundesverlag, Wien, p. 207.
Kennedy, D., 1996. Aerial archaeology in the Middle East. AARG News 12, 11–15.
Lasaponara, R., Masini, N. (Eds.), 2012. Satellite Remote Sensing: a New Tool for Archaeology. Remote Sensing and Digital Image Processing, vol. 16. Springer, Dordrecht, p. 364 xviii.
Liu, J.-G., Mason, P.J., 2009. Essential Image Processing and GIS for Remote Sensing, vol. xvi. Wiley-Blackwell, Chichester, p. 443.
Merola, P., 2005. Tecniche di telerilevamento iperspettrale applicate alla ricerca archeologica. Il caso di Lilybaeum. Archeologia Aerea. Studi Aerotopogr. Archeol. 1, 301–317.
Merola, P., Guglietta, D., Sampieri, S., Allegrini, A., 2007. Applicazione degli indici di vegetazione per lo studio di aree archeologiche. In: Atti della 11° conferenza nazionale ASITA, Torino, Italy. 6–9 novembre 2007. ASITA, Milano.
Merola, P., Guglietta, D., Sampieri, S., Allegrini, A., Guglietta, D., 2008. Lilybaeum reconstruction by remotely data. In: Remote Sensing for Archaeology and Cultural Heritage Management. Proceedings of the 1st International EARSeL Workshop, CNR, Rome. September 30–October 4, 2008. Arracne, Rome, pp. 71–74.
Mills, J., 2005. Bias and the world of the vertical aerial photograph. In: Brophy, K., Cowley, D.C. (Eds.), From the Air. Understanding Aerial Archaeology. Tempus, Stroud, pp. 117–126.
Moore, D.S., McCabe, G.P., 2003. Introduction to the Practice of Statistics, fourth ed., vol. xxv. W.H. Freeman and Company, New York. 828 + CD-ROM.
Neubauer, W., Doneus, M., Trinks, I., Verhoeven, G.J.J., Hinterleitner, A., Seren, S., Löcker, K., 2012. Long-term integrated archaeological prospection at the roman town of Carnuntum/Austria. In: Johnson, P., Millett, M. (Eds.), Archaeological Survey and the City, University of Cambridge Museum of Classical Archaeology Monographs, vol. 2. Oxbow Books, Oxford, pp. 202–221.
Neubauer, W., Eder-Hinterleitner, A., Seren, S., Melichar, P., 2002. Georadar in the Roman civil town Carnuntum, Austria: an approach for archaeological interpretation of GPR data. Archaeol. Prospect. 9 (3), 135–156.
Neubauer, W., Gugl, C., Scholz, M., Verhoeven, G.J.J., Trinks, I., Löcker, K., Doneus, M., Saey, T., Van Meirvenne, M., 2014. The discovery of the school of gladiators at Carnuntum, Austria. Antiquity 88 (339), 173–190.
Palmer, R., 2005. If they used their own photographs they would not take them like that. In: Brophy, K., Cowley, D.C. (Eds.), From the Air. Understanding Aerial Archaeology. Tempus, Stroud, pp. 94–116.
Palmer, R., 2007. Seventy-five years v. ninety minutes: implications of the 1996 bedfordshire vertical aerial survey on our perceptions of clayland archaeology. In: Mills, J., Palmer, R. (Eds.), Populating Clay Landscapes. Tempus, Stroud, pp. 88–103.
Pietrapertosa, C., Vellico, M., Sterzai, P., Coren, F., 2008. Remote sensing applied to the detection of archaeological buried structures in the aquileia site. In: Proceedings of the 27° Convegno Nazionale GNGTS - 2008, Trieste, Italia. 6-l 8 ottobre 2008, pp. 368–372.
Saey, T., Van Meirvenne, M., Trinks, I., De Smedt, P., Verhoeven, G.J.J., Neubauer, W., 2013. Integrating multi-receiver EMI measurements to characterize the soil-landscape around the school of gladiators, Carnuntum. In: Archaeological Prospection. Proceedings of the 10th International Conference on Archaeological Prospection, Vienna, Austria. May 29th – June 2nd 2013. Austrian Academy of Sciences, Vienna, pp. 430–432.
Seren, S., Eder-Hinterleitner, A., Neubauer, W., Löcker, K., Melichar, P., 2007. Extended comparison of different GPR systems and antenna configurations at the Roman site of Carnuntum. NSG 5 (6), 389–394.
The MathWorks, 2013. MATLAB E2013a Documentation – Gamma Distribution. http://www.mathworks.de/de/help/stats/gamma-distribution.html (accessed 22.03.13).
The MathWorks, 2014. Normal Parameter Estimates – MATLAB Normfit. The MathWorks. http://www.mathworks.de/de/help/stats/normfit.html (accessed 28.03.14.).
Traviglia, A., 2005. A semi-empirical index for estimating soil moisture from MIVIS data to identify subsurface archaeological sites. In: Atti della 9a Conferenza Nazionale ASITA, Catania, Italy. 15-18 novembre 2005. ASITA, Milano, pp. 1969–1974.
Traviglia, A., 2006a. Archaeological usability of hyperspectral images: successes and failures of image processing techniques. In: From Space to Place. Proceedings of the 2nd International Conference on Remote Sensing in Archaeology, CNR, Rome, Italy. December 4–7, 2006. Archaeopress, Oxford, pp. 123–130.
Traviglia, A., 2006b. MIVIS hyperspectral sensors for the detection and GIS supported interpretation of subsoil archaeological sites. In: CAA 2006: Digital Discovery. Exploring New Frontiers in Human Heritage, Fargo, ND, USA. April 2006.
Traviglia, A., 2008. The combinatorial explosion: defining procedures to reduce data redundancy and to validate the results of processed hyperspectral images. In: Remote Sensing for Archaeology and Cultural Heritage Management. Proceedings of the 1st International EARSeL Workshop, CNR, Rome. September 30–October 4, 2008. Arracne, Rome, pp. 85–89.
Trinks, I., Neubauer, W., Doneus, M., 2012. Prospecting archaeological landscapes. In: Progress in Cultural Heritage Preservation. Proceedings of the 4th International Conference, EuroMed 2012. Euromed2012, Lemessos, Cyprus. October 29–November 3, 2012. Springer, Berlin, Heidelberg, pp. 21–29.
Verhoeven, G.J.J., 2009. Beyond Conventional Boundaries: New Technologies, Methodologies, and Procedures for the Benefit of Aerial Archaeological Data Acquisition and Analysis, vol. xlii. Nautilus Academic Books, Zelzate, p. 347 (PhD thesis).
Verhoeven, G.J.J., 2012a. Near-infrared aerial crop mark archaeology: from its historical use to current digital implementations. J. Archaeol. Method Theory 19 (1), 132–160.
Verhoeven, G.J.J., 2012b. Rethinking the spectrum – the digital (R)evolution in archaeological aerial reconnaissance. In: Johnson, P., Millett, M. (Eds.), Archaeological Survey and the City, University of Cambridge Museum of Classical Archaeology Monographs, vol. 2. Oxbow Books, Oxford, pp. 45–67.
Verhoeven, G.J.J., Doneus, M., 2011. Balancing on the borderline – a low-cost approach to visualize the red-edge shift for the benefit of aerial archaeology. Archaeol. Prospect. 18 (4), 267–278.

Verhoeven, G.J.J., Doneus, M., Atzberger, C., Wess, M., Ruš, M., Pregesbauer, M., Briese, C., 2013. New approaches for archaeological feature extraction of airborne imaging spectroscopy data. In: Archaeological Prospection. Proceedings of the 10th International Conference on Archaeological Prospection, Vienna, Austria. May 29th – June 2nd 2013. Austrian Academy of Sciences, Vienna, pp. 13–15.

White, D.A., 2003. AVIRIS and archaeology in southern Arizona. In: AVIRIS Proceedings.

Wilson, D.R., 2000. Air Photo Interpretation for Archaeologists, second ed. Tempus, Stroud, p. 256.

Winterbottom, S.J., Dawson, T., 2005. Airborne multi-spectral prospection for buried archaeology in mobile sand dominated systems. Archaeol. Prospect. 12 (4), 205–219.

ZAMG, 2014. http://www.zamg.ac.at/cms/de/klima/klima-aktuell/jahresrueckblick (accessed 21.06.14.).

Zuiderveld, K., 1994. Contrast limited adaptive histogram equalization. In: Heckbert, P.S. (Ed.), Graphics Gems IV. Academic Press Professional, Boston, pp. 474–485.